



저작자표시-비영리-변경금지 2.0 대한민국

이용자는 아래의 조건을 따르는 경우에 한하여 자유롭게

- 이 저작물을 복제, 배포, 전송, 전시, 공연 및 방송할 수 있습니다.

다음과 같은 조건을 따라야 합니다:



저작자표시. 귀하는 원저작자를 표시하여야 합니다.



비영리. 귀하는 이 저작물을 영리 목적으로 이용할 수 없습니다.



변경금지. 귀하는 이 저작물을 개작, 변형 또는 가공할 수 없습니다.

- 귀하는, 이 저작물의 재이용이나 배포의 경우, 이 저작물에 적용된 이용허락조건을 명확하게 나타내어야 합니다.
- 저작권자로부터 별도의 허가를 받으면 이러한 조건들은 적용되지 않습니다.

저작권법에 따른 이용자의 권리는 위의 내용에 의하여 영향을 받지 않습니다.

이것은 [이용허락규약\(Legal Code\)](#)을 이해하기 쉽게 요약한 것입니다.

[Disclaimer](#)

**A Dissertation for the Degree of Master of Science
in Mechanical and Automotive Engineering**

**Multiscale modeling for prediction of residual stress in
additively manufactured functionally graded material**

**School of Mechanical Engineering
Graduate School
University of Ulsan**

By

Zhengtong Shan

Advisor Professor Doo-Man Chun

Co-advisor Professor Dong-Kyu Kim

June 2022

**Multiscale modeling for prediction of residual stress in
additively manufactured functionally graded material**

Advisor Professor Doo-Man Chun

Co-advisor Professor Dong-Kyu Kim

**Submitted to
the Graduate School of the University of Ulsan
in Partial Fulfillment of the Requirements
for the Degree of
Master of Science in Mechanical and Automotive Engineering**

June 2022

**School of Mechanical Engineering
Graduate School
University of Ulsan**

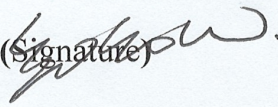

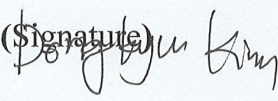
**By
Zhengtong Shan**

To Approve the Submitted Dissertation for the Degree of
Master of Science in Mechanical and Automotive Engineering

By
Zhengtong Shan

**Title: Multiscale modeling for prediction of residual stress in additively
manufactured functionally graded material**

August 2022

Committee Chair	Professor Kyongsik Chang	(Signature) 
Committee	Professor Doo-Man Chun	(Signature) 
Committee	Professor Dong-Kyu Kim	(Signature) 

Graduate School

University of Ulsan, South Korea

ABSTRACT

Multiscale modeling for prediction of residual stress in additively manufactured functionally graded material

Zhengtong Shan

School of Mechanical Engineering

Graduate School

University of Ulsan

(Supervised by Professor Doo-Man Chun and Professor Dong-Kyu Kim)

In the present study, a multiscale modeling based on the inherent strain method was proposed for fast prediction of residual stress distribution in functionally graded material (FGM). The inherent strains of individual composition were defined by thermo-mechanical analysis with actual process parameters in a meso-scale model. Then the corresponding inherent strains in each composition was mapped continuously to a macro-scale model in the static mechanical analysis to obtain the residual stress distribution. Four types of specimens with different gradient paths and scanning strategies were prepared by directed energy deposition. The contour method, neutron diffraction and deep hole drilling were performed to measure the residual stress. The inherent strains of the composition composed of 50% 316L and 50% P21 powders were found that has

smallest magnitude among the calculated compositions instead of exhibiting a gradual variation with the change of chemical composition. It was proved to be responsible for the fluctuation in the sine-wave-like stress profiles in FGM structure. The effect of different lumping layer method for mapping the inherent strain to each composition layer on residual stress was also investigated and the results with selected layer lumping final showed an excellent agreement with the experimental results. For the computational efficiency, the total calculation time for each FGM structure with different gradient path is significantly reduced.

ACKNOWLEDGEMENTS

On the occasion of the finalization of this dissertation, I would like to express my sincere appreciation to the people who provide me with their help during the past two years. Without their help this dissertation would never be finished.

I would like to express my special appreciations of gratitude to Professor Doo-Man Chun and Professor Dong-Kyu Kim, my advisors, for their patience, suggestions, encouragement and guidance during my Master program. Since thanks are also extended to the members of the committee member, Prof. Kyoungsik Chan, for his valuable comments. Also, I would like to thank other professors who had taught me in the school of Mechanical Engineering.

Specially, I want to express my gratitude to the members of the Computational Advanced Material Processing Laboratory of University of Ulsan, who are Mr. Minh Tien Tran, Mr. Dae-Ho Lee, Mr. Tri Hoang Nguyen, Mr. Minh Sang Pham for their fruitful opinions, ideas and directions for my research and daily life.

More thanks are extended to my friends, Yu Shen, Ge Cao, Yue Teng and Haoyue Wu for daily helps. We had a great time at school together.

Finally, I would like to express my sincere gratitude to my family for their endless support, understanding, encouragement and patience for me during my studies.

TABLE OF CONTENTS

ABSTRACT	i
ACKNOWLEDGEMENTS	iii
LIST OF FIGURES	vi
LIST OF TABLES	viii
CHAPTER 1	1
INTRODUCTION	1
1.1. Additively-manufactured functionally graded material	1
1.2. Prediction of residual stress	1
1.3. Research objectives	3
CHAPTER 2	5
EXPERIMENTAL PROCEDURE	5
2.1. Directed energy deposition	5
2.2. Macrostructure measurement and mechanical testing	6
2.3. Residual stress measurements	7
CHAPTER 3	8
SIMULATION OF DIRECT ENERGY DEPOISTION PROCESS	8
3.1. Multiscale modeling	8
3.2. Meso-scale modeling	8
3.2.1 Calculation of thermo-physical properties	8
3.2.2 Thermo-mechanical analysis	10
3.2.3 Modeling conditions of meso-scale model	12
3.2.4 Extracting inherent strain	13
3.2.5 Procedure of thermo-mechanical simulation	14
3.3. Macro-scale modeling	16
3.3.1 Mapping inherent strain to FGM	16
3.3.2 Modeling conditions of Macro-scale model	17

CHAPTER 4	20
RESULTS AND DISCUSSION	20
4.1. Material properties of each composition	20
4.2. Validation of thermal model	22
4.3. Inherent strains of each composition	23
4.4. Lumping layer method in case I	25
4.5. Residual stress and thermal distortion	27
CHAPTER 5	32
CONCLUSIONS	32
REFERENCES	34

LIST OF FIGURES

Fig. 2. 1 Schematic of functionally graded material (FGM) structures fabricated by direct energy deposition (DED): (a) Case I, no interlayer with bidirectional scan, (b) Case II, one interlayer with bidirectional scan, (c) Case III, three interlayers with bidirectional scan, (d) Case IV, three interlayers with orthogonal scan.

Fig. 3. 1 Illustration of multiscale modeling in FGM processed by AM

Fig. 3. 2 (a) Meso-scale finite element model for thermo-mechanical analysis and (b) illustration of measuring paths for extracting the inherent strain

Fig. 3. 3 Procedure of creating heat source model

Fig. 3. 4 Procedure of setting model change

Fig. 3. 5 Procedure of defining the pre-temperature field

Fig. 3. 6 (a) Procedure of setting the equivalent thermal expansion coefficients and (b) procedure of applying the unitary temperature change in each layer

Fig. 3. 7 Macro-scale finite element model: (a) boundary conditions and schematic of layer lumping method with (b) single numerical layer (1N), (c) 2 numerical layers (2N), (d) 3 numerical layers (3N) and (e) 6 numerical layers (6N).

Fig. 4. 1 The coefficient of thermal expansion (CTE) of each composition in case III compared between the experimental and calculated results.

Fig. 4. 2 Melting pool sizes and morphologies of FGM structure by (a, c) macrostructure measurement and (b, d) simulation results for 316L and P21, respectively.

Fig. 4. 3 The plastic strain distributions in (a) TD, (b) BD and (c) LD along different passes of three compositions

Fig. 4. 4 The inherent strains of each composition along the TD, BD and LD

Fig. 4. 5 (a) Two-dimensional mapping of the residual stress distributions in LD obtained by contour method, and (b) predicted cross-sectional residual stress distribution in the FGM for case I by different layer lumping strategies.

Fig. 4. 6 Residual stress distributions of the FGM for case I along the TD, BD and LD obtained from the measuring path as indicated in Fig. 9.

Fig. 4. 7 Through-thickness distributions of longitudinal stress obtained by neutron diffraction, contour method, deep hole drilling and multiscale simulation: (a) case I, (b) case II, (c) case III, and (d) case IV.

Fig. 4. 8 (a) Schematic of the new gradient path without the 50% 316L composition, and (b) Longitudinal residual stress distributions of two gradient paths (with and without 50% 316L composition)

Fig. 4. 9 (a) Distortion field of case I and distortion profiles: (b) case I, (c) case II, (d) case III and (e) case IV.

Fig. 4. 10 The computational time of the coupled thermo-mechanical analysis on the 3-layer meso-scale model and mapping inherent strains to different case

LIST OF TABLES

Table 3. 1 The chemical composition of different powder alloys in the present study

Table 4. 1 Temperature-dependent thermophysical properties of P21

CHAPTER 1

INTRODUCTION

1.1. Additively-manufactured functionally graded material

Functionally graded material (FGM) is defined as a class of material with the gradual variation of properties and functions by changing the compositions or microstructure, which could be manufactured for specific applications and situations [1,2]. It could replace traditional dissimilar structures which may cause stress corrosion cracking and harmful residual stress due to the sharp changes in chemical composition and material properties [2].

In the fabrication of FGM, compared with conventional manufacturing methods including vapor deposition technique [3], powder metallurgy [4], spark plasma sintering [5], and centrifugal casting [6], additive manufacturing (AM) has drawn much attention due to its unique advantages in fabricating geometrically complex components or customized part [7–12]. With the enormous potential for rapid production of geometrical complex, lightweight and customized metallic parts, 3D printing is making a giant breakthrough in the fields of aviation, bio-medical and renewable energy.

1.2. Prediction of residual stress

However, the large thermal gradient and rapid solidification during AM process can lead to a high residual stress and excessive thermal distortion, consequently resulting in the poor mechanical behavior of product or even part failure [13]. Various experiments have been performed to evaluate residual stress and investigate the effect of different processing strategies such as neutron

diffraction [14–16], x-ray diffraction [17] and contour/hole drilling method [18], [19]. The limits of these experiments are generally expensive and time-consuming. Therefore, it is necessary to develop numerical modeling for prediction of residual stress and processing parameters optimization. In AM simulations, thermo-mechanical analysis based on finite element method originally used for metal welding process has already been widely developed and implemented in residual stress and distortion predictions [20,21]. Despite the detailed analysis on a high-fidelity model with real process parameters could achieve accurate prediction, it is limited to apply for small scale model since the multi-physics problem involving transient heat transfer and non-linear mechanical deformation brings large computation cost. Especially in AM, the real process usually contains thousands of layers. In order to make AM simulation more efficient, several simplified methods and assumptions have been developed. For instance, some researches focused on reducing the element size by adaptive mesh refinement [22,23], others paid attention to simplify scanning strategy through applying equivalent heat source [24,25].

Besides, inherent strain method (ISM) which was proposed for fast estimation of residual stress in welding has become one of the most common and efficient approach [26–28]. The inherent strain is obtained from thermo-mechanical analysis of small size specimen firstly and then applied to the real size part through a simple linear elastic calculation. Liang et al. [29–33], developed a modified inherent strain method based on multiscale modeling for residual stress and distortion predictions which the change of mechanical boundaries due to deposition is taken into account. Setien et al. [34] presented an empirical methodology to determine the inherent strain based on classical laminate theory. Wang et al. [35] proposed a modified inherent strain method considering the variance of the mechanical properties in applying the inherent strain.

1.3. Research objectives

To date, most of studies have been investigated modeling methods for residual stress prediction in the single alloy components, while few researches have focused on predicting the residual stress of FGM structures in AM. In comparison with single alloy material, the characteristic of FGM is the different thermo-physical properties of various compositions which may bring the interactions among the intermediate parts. It can affect the temperature history and evolution of residual stress of the entire structure. Thermo-mechanical modeling has been utilized for FGM structure to obtain accurate temperature field and residual stress distribution of some structures [36–38]. Nevertheless, for defining the optimal gradient path of composition in the FGM conceptual design, it is not efficient to implement repeatedly many thermo-mechanical analyses to understand the effects of each composition and processing parameters on the residual stress.

In the present research, we proposed a multiscale modeling based on inherent strain method for the prediction of residual stress and distortion of FGM more efficient. The thermo-mechanical analyses were only conducted on a meso-scale model to determine the inherent strains of different compositions which could be regarded as constant with the same processing parameters. Hence, for the structures with different gradient paths, the corresponding inherent strains could be mapped directly instead of continuously repeating the thermal-mechanical analysis. For further reduction of the computational cost, different lumping layer methods were applied in the macro-scale model and the accuracy and efficiency were evaluated. By comparing the variation of inherent strains with the change of chemical composition, the effect of individual composition layer on the residual stress of each FGM structure was also investigated. To validate the proposed model, the contour method, neutron diffraction and deep hole drilling were performed to measure the residual stress distributions in the four types of FGM specimens with variation of 316L and P21 powders prepared

by directed energy deposition (DED). During the experiment, the thermo-physical material properties such as yield strength (YS) and coefficient of thermal expansion (CTE) were obtained. Then, the results were used to verify the calculated YS and CTE by thermodynamic calculations based on the chemical compositions.

CHAPTER 2

EXPERIMENTAL PROCEDURE

2.1. Directed energy deposition

Austenitic stainless steel powder (316L) and ferritic carbon steel powder (P21) with the particle size of 45-150 μm were prepared. Then, the specimens were manufactured by DED process using an INSSTEK MX-400 equipment under an inert argon gas atmosphere with a pressure of 10 mbar and an oxygen level of 0.2%. The DED process was performed with a laser power of 200–1000 W, a scanning speed of 14.1 mm/s, a layer thickness of 250 μm , and a hatch width (laser beam spot size) of 400 μm . As depicted in Fig. 2.1, there are four cases of rectangular specimens which were fabricated on a ferritic steel substrate (S45C). Figs. 1(a-c) show different gradient paths of composition with a zig-zag scanning strategy starting from the same location among different layers. Fig. 2.1(a) shows the schematic of case I which consists of two interlayers with equal composition of 100 wt% austenitic and ferritic steel. As shown in Figs. 2.1(b, c), one interlayer of 50% austenitic and 50% ferritic steel and three interlayers with a linear increment of 25 wt% of P21 from bottom were added in case I and case II, respectively. The case IV (Fig. 2.1 (d)) is the same structure as case III with orthogonal scanning strategy.

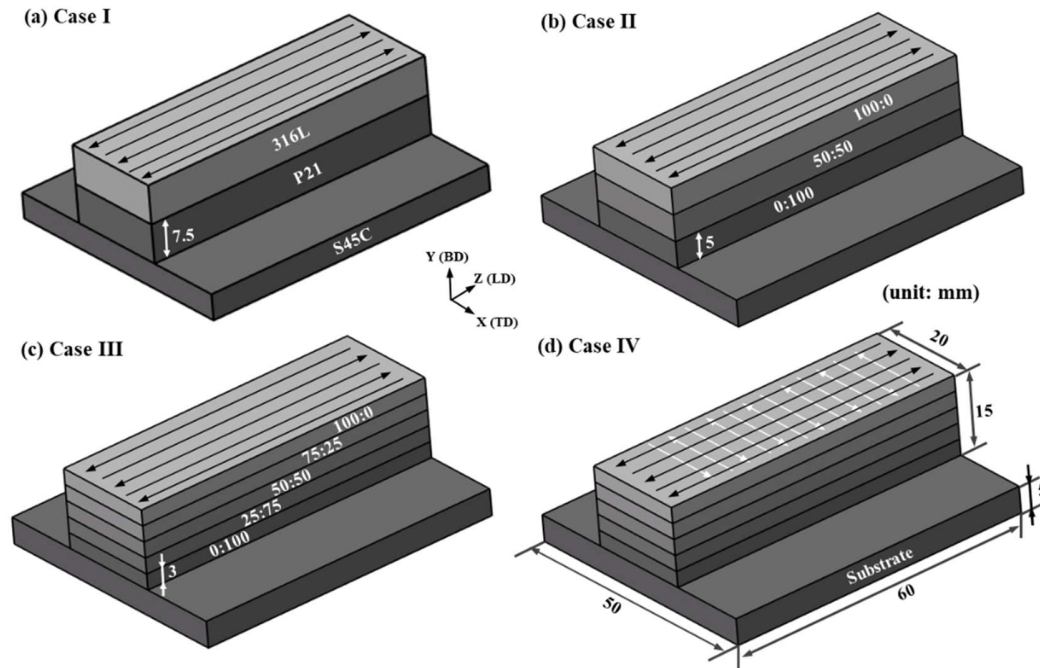


Fig. 2. 1 Schematic of functionally graded material (FGM) structures fabricated by direct energy deposition (DED): (a) Case I, no interlayer with bidirectional scan, (b) Case II, one interlayer with bidirectional scan, (c) Case III, three interlayers with bidirectional scan, (d) Case IV, three interlayers with orthogonal scan.

2.2. Macrostructure measurement and mechanical testing

The specimens for microstructural characterization were prepared via cutting with electrical discharge machining (EDM) in the cross-section perpendicular to the LD. Macrostructure observation were performed by optical microscopy (OM) after electrolytic etching using an etchant of 10% perchloric acid and 90% acetic acid. Uniaxial tensile testing was conducted at room temperature under an initial strain rate of 10^{-3} s^{-1} using a dynamic universal materials testing machine (MTS landmark 100). In addition, thermal expansion coefficient was also obtained through thermal dilation experiments.

2.3. Residual stress measurements

Three orthogonal stress components in each FGM structure were provided by neutron diffraction. Spatially-resolved neutron strain mapping was conducted by using the KOWARI engineering strain diffractometer at ANSTO. And diffraction peak positions were determined by a least squares Gaussian fitting method using instrumental data analysis programs. Contour method was implemented for obtaining the two-dimensional stress map. The specimens were cut in half at the mid-length position by using EDM with a 100 μm diameter brass wire. After cutting, the normal direction (x) displacements on the cut surfaces were measured using a scanning confocal laser probe. The measured displacements were applied inversely to an assumed flat surface contour using an elastic finite element (FE) model to calculate the residual stress. For the high magnitude and tri-axial residual stresses in FGM specimens, the incremental deep hole drilling method was applied for longitudinal and transverse stress measurements through the thickness of the specimens. The characteristic of this method is that the core is extracted in incremental machining steps and the diameter of the reference hole is measured between each increment.

CHAPTER 3

SIMULATION OF DIRECT ENERGY DEPOSITION PROCESS

3.1. Multiscale modeling

Firstly, as shown in Fig. 3.1, the inherent strains of each composition layer such as 50% 316L are determined from the meso-scale model based on thermo-mechanical analysis considering the actual material properties, processing parameters and scanning strategies. Then mapping the inherent strains to the corresponding part (red area) of the macro-scale models with different gradient paths is achieved by a layer-by-layer activation from bottom to up.

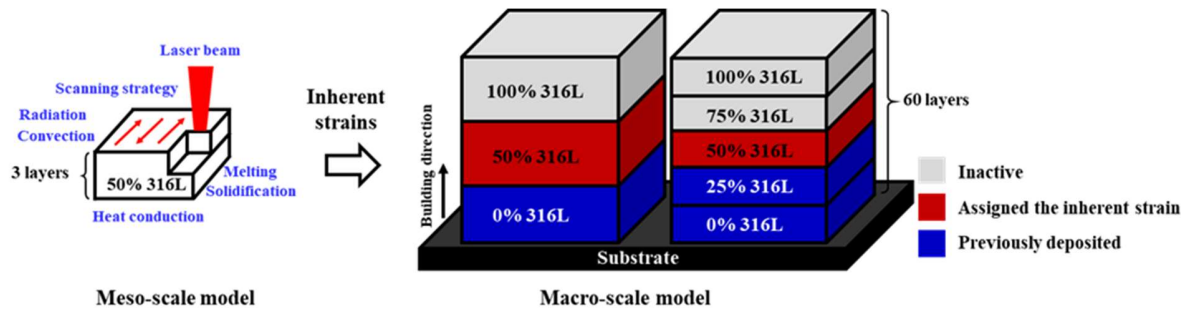


Fig. 3. 1 Illustration of multiscale modeling in FGM processed by AM

3.2. Meso-scale modeling

3.2.1 Calculation of thermo-physical properties

In FGM, temperature-dependent material properties of each composition are essential to perform accurately the thermo-mechanical analysis. Due to the large range of temperature and various kinds of alloying element contents, however, it is difficult to obtain through experiments directly or take from the available reference. Thus, a numerical model based on thermodynamic

calculations was implemented for defining the thermo-physical properties using JmatPro [36,41], [41]. The equilibrium fraction of phases should be determined firstly and relevant properties for each phase are computed based on the alloy constitution. The property of each phase is expressed as follows

$$P = \sum_i x_i P_i^0 + \sum_i \sum_{j>i} x_i x_j \sum_v \Omega_{ij}^v (x_i - x_j)^v \quad (1)$$

where P is the property of the phase and P_i^0 is the property of the phase in the pure element. x_i and x_j are the mole fractions of i and j in the phase, respectively. Ω_{ij}^v is a binary interaction parameter between elements i and j dependent on v . The effects of temperature on the properties are taken into account by temperature-dependent values, P_i^0 and Ω_{ij}^v . Then the final property of alloy can be calculated by a generalized law of mixtures according to the phase fractions and properties of individual phase [42]. As given in Table 3.1, the chemical compositions of 316L and P21 alloy powders for different parts were used for the calculation of thermo-physical properties of FGM structure. The calculated results were calibrated by the experimental measurements.

Table 3. 1 The chemical composition of different powder alloys in the present study

	C	Si	Mn	P	S	Cr	Ni	Mo	V	Al	Fe
316L: P21 = 1:0	0.03	0.75	2	0.05	0.03	17	12	2.5	-	-	65.65
316L: P21 = 3:1	0.073	0.638	1.575	0.045	0.03	12.85	10	1.875	0.05	0.288	72.585
316L: P21 = 1:1	0.115	0.525	1.15	0.04	0.03	8.7	8	1.25	0.1	0.575	79.515
316L: P21 = 1:3	0.158	0.413	0.725	0.035	0.03	4.55	6	0.625	0.15	0.863	86.455
316L: P21 = 0:1	0.2	0.3	0.3	0.03	0.03	0.4	4	0	0.2	1.15	93.39

3.2.2 Thermo-mechanical analysis

In thermal analysis, the governing equation is the heat conduction equation, which can be expressed as:

$$\rho C_p \frac{\partial T}{\partial t} = \frac{\partial}{\partial x} \left(k \frac{\partial T}{\partial x} \right) + \frac{\partial}{\partial y} \left(k \frac{\partial T}{\partial y} \right) + \frac{\partial}{\partial z} \left(k \frac{\partial T}{\partial z} \right) + Q \quad (2)$$

where ρ , C_p , and k depending on the temperature are the material density, specific heat and thermal conductivity, respectively. T is the temperature; t is the time; Q is the internal heat source. x , y , and z are the global coordinates of the material point.

The internal heat source Q is approximated by the double ellipsoidal model [43]:

$$q = \frac{6\sqrt{3}f_1Q_e}{abc_f\pi\sqrt{\pi}} \exp\left(-3\frac{z^2}{c_f^2} - 3\frac{x^2}{a^2} - 3\frac{y^2}{b^2}\right) \quad z \geq 0 \quad (3)$$

$$q = \frac{6\sqrt{3}f_2Q_e}{abc_r\pi\sqrt{\pi}} \exp\left(-3\frac{z^2}{c_r^2} - 3\frac{x^2}{a^2} - 3\frac{y^2}{b^2}\right) \quad z < 0 \quad (4)$$

where q is the heat energy density and Q_e is the effective power. f_1 and f_2 are fractions of the heat deposited in the front and rear of the ellipsoid, which satisfy the dependence $f_1 + f_2 = 2$. a , b , c_f , and c_r are respectively the half-width, depth, the front and rear half-length of the heat source.

Initial condition and boundary conditions can be expressed as:

$$T(x, y, z)_{t=0} = T_0 \quad (5)$$

$$k \frac{\partial T}{\partial \mathbf{n}} = q - q_c - q_r \quad (x, y, z) \in S \quad (6)$$

where T_0 is the initial temperature, S is the boundary surface, and \mathbf{n} is normal vector of S . The convection and radiation are considered in heat losses, which can be defined by:

$$q_c = h(T - T_e) \quad (7)$$

$$q_r = \sigma \varepsilon (T^4 - T_e^4) \quad (8)$$

where h , σ , and ε are the heat convection coefficient, Stefan-Boltzmann constant, and emissivity, respectively. T_e is the environment temperature.

In mechanical analysis, the governing equation is the mechanical equilibrium equation given by Eq. (9).

$$\nabla \cdot \boldsymbol{\sigma} + \mathbf{b} = 0 \quad (9)$$

where $\boldsymbol{\sigma}$ is the stress tensor and \mathbf{b} is the body force.

The elastoplastic material constitutive model with von Mises yield criterion can be described as:

$$\boldsymbol{\sigma} = C(\boldsymbol{\varepsilon} - \boldsymbol{\varepsilon}_p - \boldsymbol{\varepsilon}_t) \quad (10)$$

$$\boldsymbol{\varepsilon}_t = \alpha \cdot \Delta T \quad (11)$$

$$\sigma_v = \sqrt{\frac{(\sigma_1 - \sigma_2)^2 + (\sigma_2 - \sigma_3)^2 + (\sigma_3 - \sigma_1)^2}{2}} \quad (12)$$

where C represents the fourth-order stiffness tensor; ε , ε_p , ε_t and α are respectively the total strain, plastic strain and thermal strain. α is the thermal expansion coefficient and ΔT is the change in temperature. σ_v represents the equivalent stress; σ_1 , σ_2 , and σ_3 are principal stress in different directions.

3.2.3 Modeling conditions of meso-scale model

For obtaining different inherent strains of each composition, a meso-scale model was proposed to perform thermo-mechanical analysis using Abaqus. The meso-scale FE model is shown in Fig. 3.2. Fig. 3.2 (a) shows a 3-layer deposition part in dimension of $8 \times 1.6 \times 0.75 \text{ mm}^3$, which was built on a building platform with a relatively large dimension. Considering the bidirectional scanning strategy, only the length of deposition layer (longitudinal direction) should be set to ensure the temperature field can reach the steady state in each single pass deposition. And building platform with relatively large size was designed to avoid the high thermal accumulation in deposition layer. It only increases a little bit computational burden because the majority of the platform area is far away from the large temperature gradient region. In addition, the same material is applied for the deposition part and building platform to prevent the influence of dissimilar material.

In transient heat transfer analysis, the modeling parameters was determined by the experimental conditions as described in Section 2.1. The melting pool generated by double ellipsoidal model was modified to match the shape of melt pool in cross-sectional micrographs through adjusting the parameters in Eqs. (3, 4). The initial temperature was set as same as environment temperature (25 °C). The heat losses including convection and radiation were applied to the surface of the model, except for the bottom of the building platform. Besides, the element birth and death were achieved through user-defined subroutines. After completing the thermal

analysis, the obtained temperature history was implemented as input for mechanical analysis. The bottom of the building platform was fully fixed as depicted in Fig. 3.2(a). The removal of the boundary conditions was simulated when the modeling was cooled down to the environment temperature.

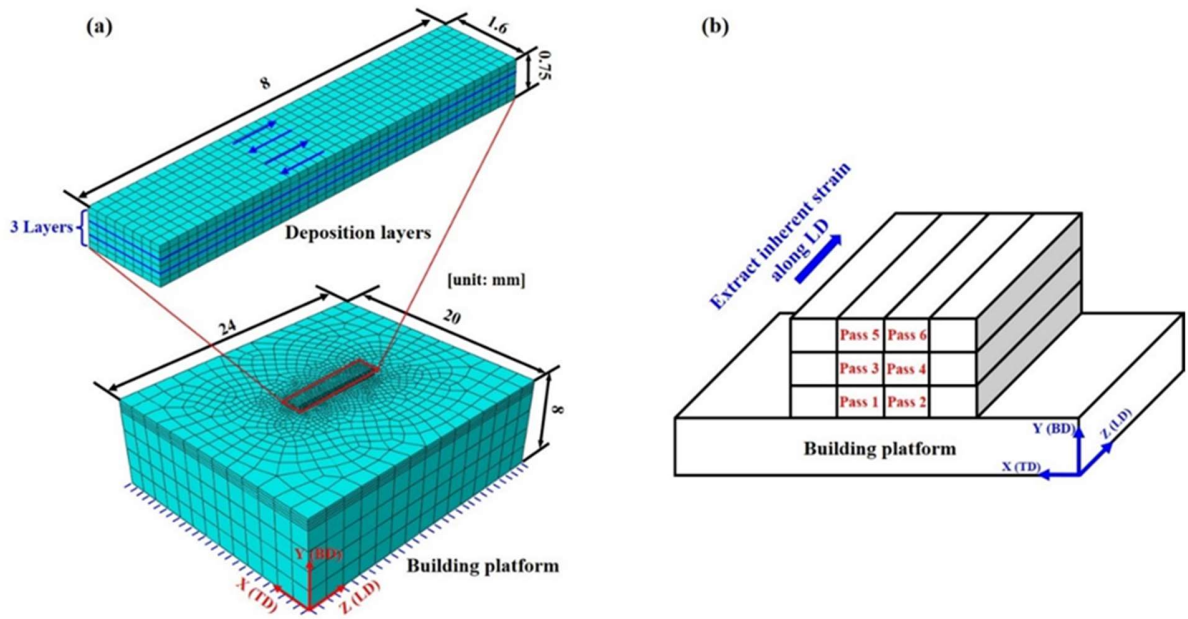


Fig. 3. 2 (a) Meso-scale finite element model for thermo-mechanical analysis and (b) illustration of measuring paths for extracting the inherent strain

3.2.4 Extracting inherent strain

The inherent strains are regarded as the unrecoverable inelastic strains after removing the mechanical constraint, which should be similar if the parts are processed under the same parameters and conditions. The equation of inherent strains ε^* can be written as:

$$\varepsilon^* = \varepsilon^{tot} - \varepsilon^e = \varepsilon^p + \varepsilon^t + \varepsilon^c + \varepsilon^{ph} \quad (13)$$

where ϵ^{tot} are the total strains, ϵ^e are the elastic strain, ϵ^p are the plastic strains, ϵ^t are thermal strains, ϵ^c are the creep strains and ϵ^{ph} are the strains caused by phase transformation. The thermal strains can be assumed to be zero since the parts are cooled down to the room temperature finally. The creep strains and strains caused by phase transformation could be also neglected if they are relatively small compared with the plastic strain. Once the thermo-mechanical analysis was finished, the distribution of plastic strain in meso-scale model could be obtained. As depicted in Fig. 3.2 (b), six passes were chosen for extracting the plastic strain distribution in three normal directions. In order to study the effect of remelting of previously deposited and thermal shrinkage of next layer on inherent strain, the comparisons of plastic strain distribution of these passes were discussed in Section 4.

3.2.5 Procedure of thermo-mechanical simulation

In this chapter, the procedure of thermos-mechanical simulation based on Abaqus software are introduced. The thermal analysis was conducted firstly to obtain the detailed thermal field. The thermal physical properties calculated by JmatPro and the heat source model should be determined as input for thermal analysis firstly. As shown in Fig. 3.3, The heat source model was coded in the subroutine of Abaqus and applied to the deposition layer as heat flux. The method of model change was layer-by-layer manner to simulate the real DED process as depicted in Fig. 3.4. After the temperature field was obtained, the thermal history was utilized as input in mechanical analysis through defining the pre-temperature field of each layer shown in Fig. 3.5.

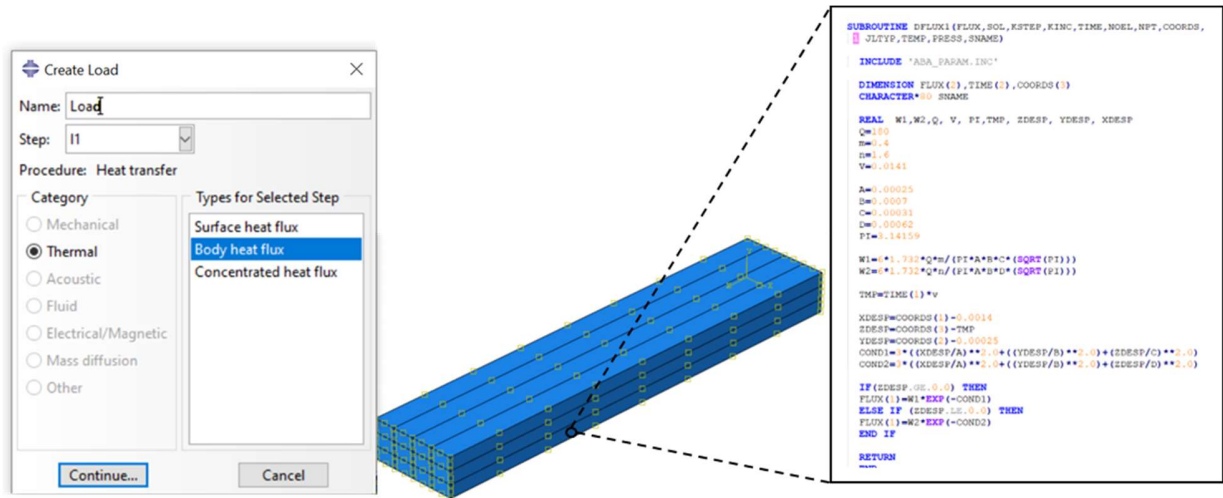


Fig. 3. 3 Procedure of creating heat source model

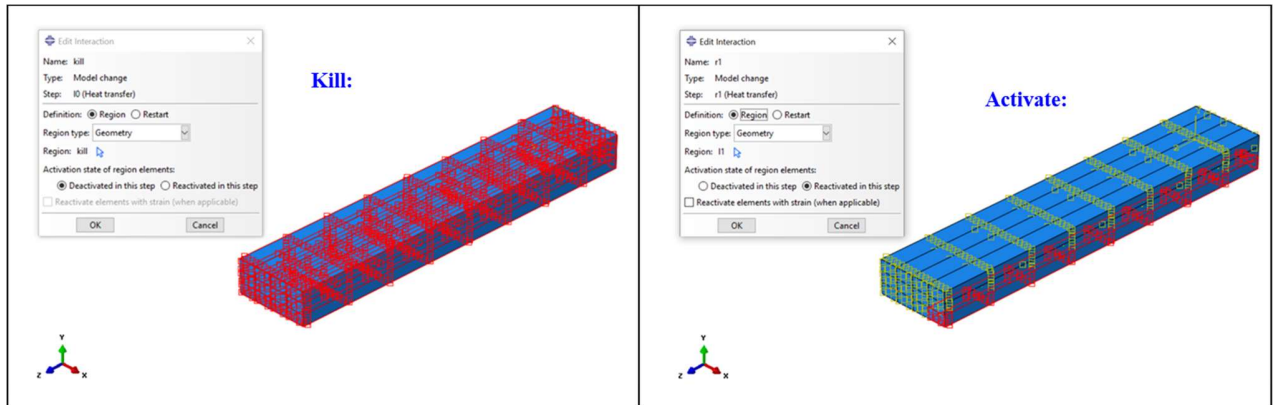


Fig. 3. 4 Procedure of setting model change

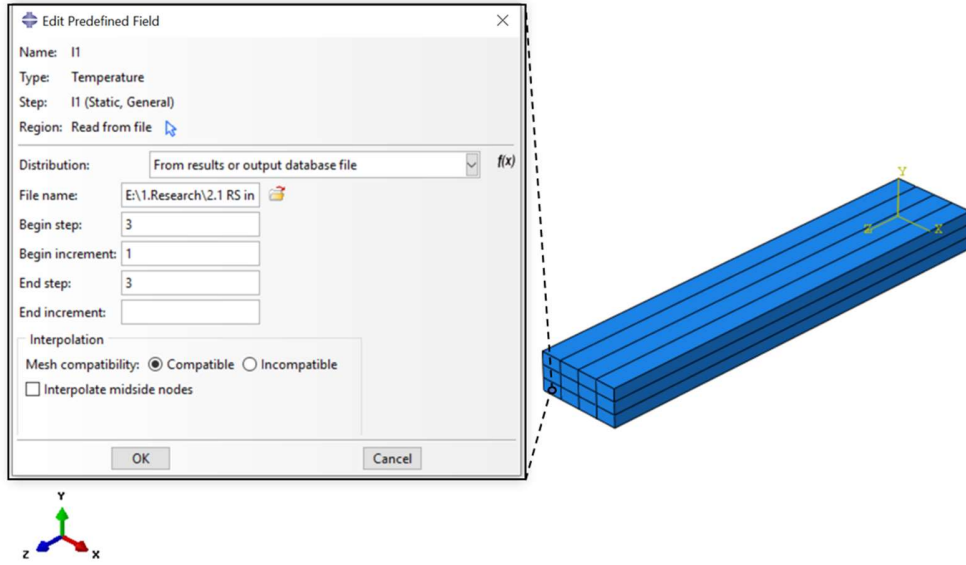


Fig. 3.5 Procedure of defining the pre-temperature field

3.3. Macro-scale modeling

3.3.1 Mapping inherent strain to FGM

The inherent strains of different compositions extracted from meso-scale modeling were applied to macro-scale modeling. As mentioned above, totally four cases of FGM structures were used for verification. These structures were sliced into several numerical layers that were activated from the bottom sequentially along the building direction using element birth and death methods. When one numerical layer was activated, the related inherent strains were applied according to the specific material through the Eq. (14).

$$\varepsilon_i^* = \alpha_i \cdot \Delta T \quad (14)$$

where α is the equivalent thermal expansion coefficient identical to the inherent strain and ΔT is the unitary temperature change. i is determined for identifying the different composition. After defining the equivalent thermal expansion coefficient in material properties, a unitary temperature

change in each layer could cause the thermal deformation sequentially. Then, the static mechanical analysis was performed to calculate the residual stress and distortion. The computational time of single simulation only takes several minutes. As depicted in Fig. 3.6, the equivalent thermal expansion coefficients were defined in material properties in Abaqus and the unitary temperature change in each layer was applied through setting the pre-temperature field of the model.

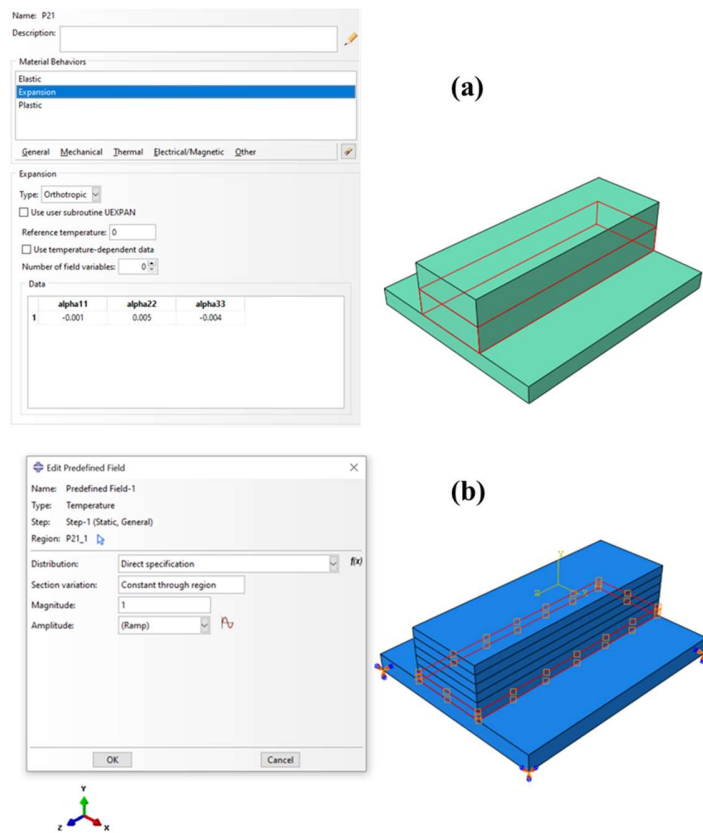


Fig. 3. 6 (a) Procedure of setting the equivalent thermal expansion coefficients and (b) procedure of applying the unitary temperature change in each layer

3.3.2 Modeling conditions of Macro-scale model

The FE model of case I was shown in Fig. 3.7. Note that the FE model for the other cases was used as same in case I. In the real DED process, the substrates were put in the building platform directly

without any constraints. Therefore, setting up redundant boundary conditions could affect the evolution of the residual stress. In the other hand, it is impossible to remove all the constraints of the model due to the stiffness matrix singularity. Considering this situation, the fully fixed boundary conditions were applied to a small area at the center of the bottom of the model as depicted in Fig. 3.7(a). The model of case I was also used to investigate the influence of layer lumping method. It could affect the evolution of the residual stress and the accuracy of prediction results. The large numerical layer thickness (NLT) may reduce the accuracy of the simulation result because of neglecting the interactions between the different composition layers whereas the small NLT can obtain the great result accuracy but bring the large computational cost at the same time. Figs. 3.7(b, e) proposed different NLT for layer lumping method in case I to define the proper value. There were 2 composition layers in case I. Each composition layer was replaced by 1,2,3 and 6 numerical layers. They were denoted by 1N, 2N, 3N and 6N respectively. The initial hexahedral element size of $1.25 \times 1.25 \times 1.25 \text{ mm}^3$ were used, while it was adjusted for the 3N and 6N to make sure each numerical layer has three mesh elements along the thickness direction denoted by 3N3E and 6N3E.

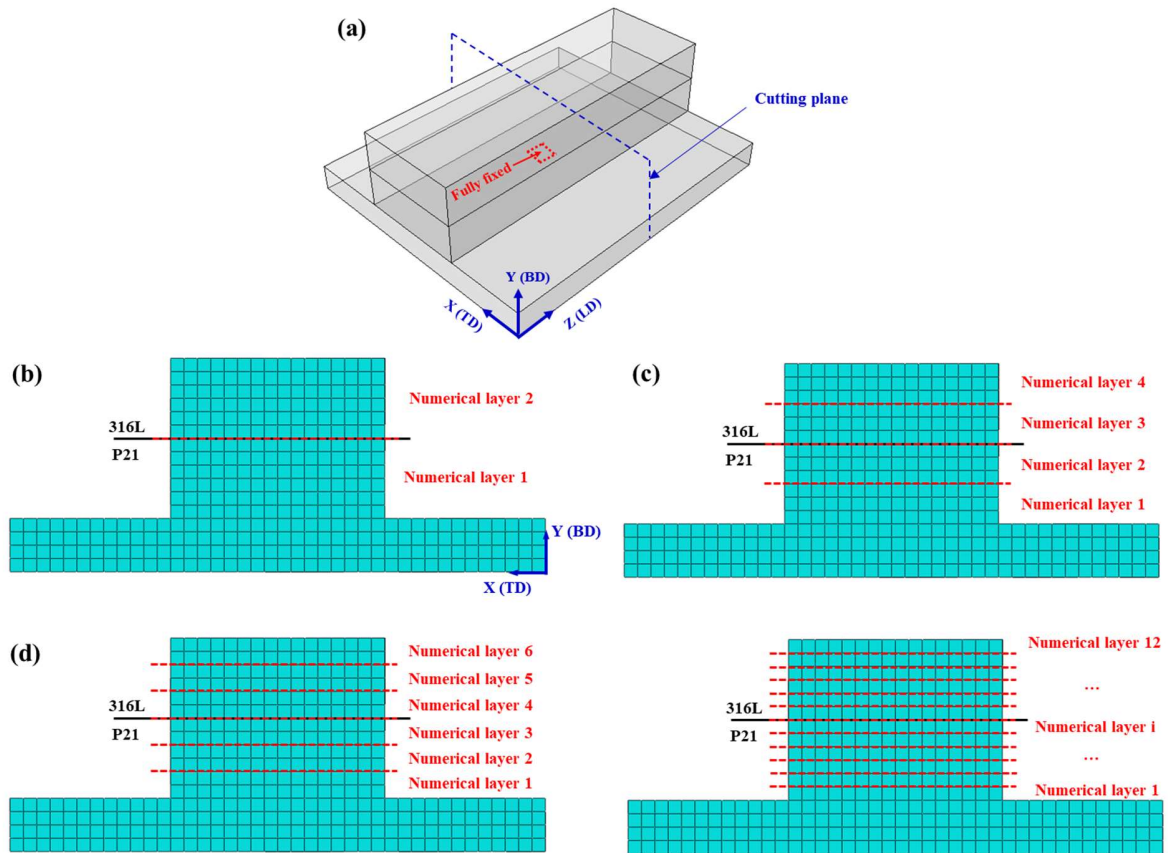


Fig. 3. 7 Macro-scale finite element model: (a) boundary conditions and schematic of layer lumping method with (b) single numerical layer (1N), (c) 2 numerical layers (2N), (d) 3 numerical layers (3N) and (e) 6 numerical layers (6N).

CHAPTER 4

RESULTS AND DISCUSSION

4.1. Material properties of each composition

The calculated thermo-physical and mechanical properties of P21 are listed in Table 4.1 and the material properties of other compositions are provided in the supplementary document. According to the calculation results of 316L as shown in Table S1 in the supplementary document, there is large mismatch of material properties such as yield stress and coefficient of thermal expansion (CTE) between the P21 and 316L which could cause harmful tensile stress along the interface of dissimilar joint. With the reduction in the austenitic steel composition, most of material properties show a gradual variation to reduce the large difference of material properties among two dissimilar materials. The variation of CTE in each composition between the experiment and calculation is shown in Fig. 4.1. It indicates the distribution of calculated CTE shows a good agreement with measured data. The difference of CTE between P21 and 316L in the FGM structure is approximately 33%. But with the increase in 316L composition to 50%, the difference of CTE is only 10% compared with P21. Moreover, for the yield stress, the value of 50% 316L shown in the Table S3 is almost identical to that of the P21 layer. The reason for this situation seemed to be the relatively fine grain size and high content of substitutional atoms in the tempered α' martensite compared with that of P21 [39]. These special material properties of 50% 316L may lead to the unexpected fluctuation in residual stress distribution of the entire structure.

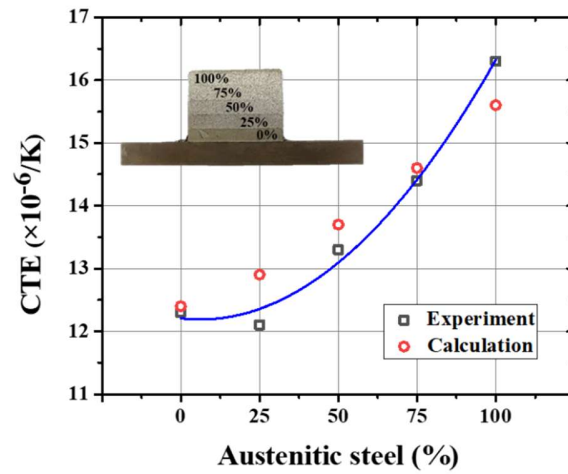


Fig. 4. 1 The coefficient of thermal expansion (CTE) of each composition in case III_ compared between the experimental and calculated results.

Table 4. 1 Temperature-dependent thermophysical properties of P21

TEMPERATURE T (K)	300	500	700	1000	1300	1600	1800	2200	3000
DENSITY, P (KG/M3)	7753	7701	7635	7526	7313	7207	6838	6494	5763
SPECIFIC HEAT, C (J/(KG·K))	460	542	653	850	631	682	812	828	829
CONDUCTIVITY, K (W/(M·K))	21.4	26.6	30.3	29.8	28.7	32.3	33.2	40.3	54.5
YOUNG'S MODULUS, E (GPA)	206	197	180	142	107	77	0.22	-	-
POISON RATIO, N	0.29	0.30	0.31	0.32	0.35	0.37	0.49	-	-
THERMAL EXPANSION, A ($\times 10^{-6}/K$)	12.4	13.1	13.9	15.5	17.9	19.6	30.3	-	-
YIELD STRESS, Σ_Y (MPA)	1148	851	101	88	84	1	1	-	-

4.2. Validation of thermal model

Figs. 4.2(a, c) represent the cross-sectional micrographs of 316L and P21, respectively. The macrostructure of other composition could be found in the previous research [40]. The interfaces between the dissimilar materials are apparent observed. The melting pool sizes and morphologies can be obtained as shown in Figs. 4.2(a, c). Comparatively short in width and deep in depth of melting pool are observed in 316L layer. The simulated shapes of the melting pool (grey area) for 316L and P21 are shown in Figs. 4.2(b, d), respectively. It reveals that the simulated results well reproduce the experimental melting pool sizes and morphologies of both 316L and P21. Besides, the temperature gradient of thermal model is also provided in the Fig. 4.2. The maximum temperature during the DED process of P21 is higher than that of 316L.

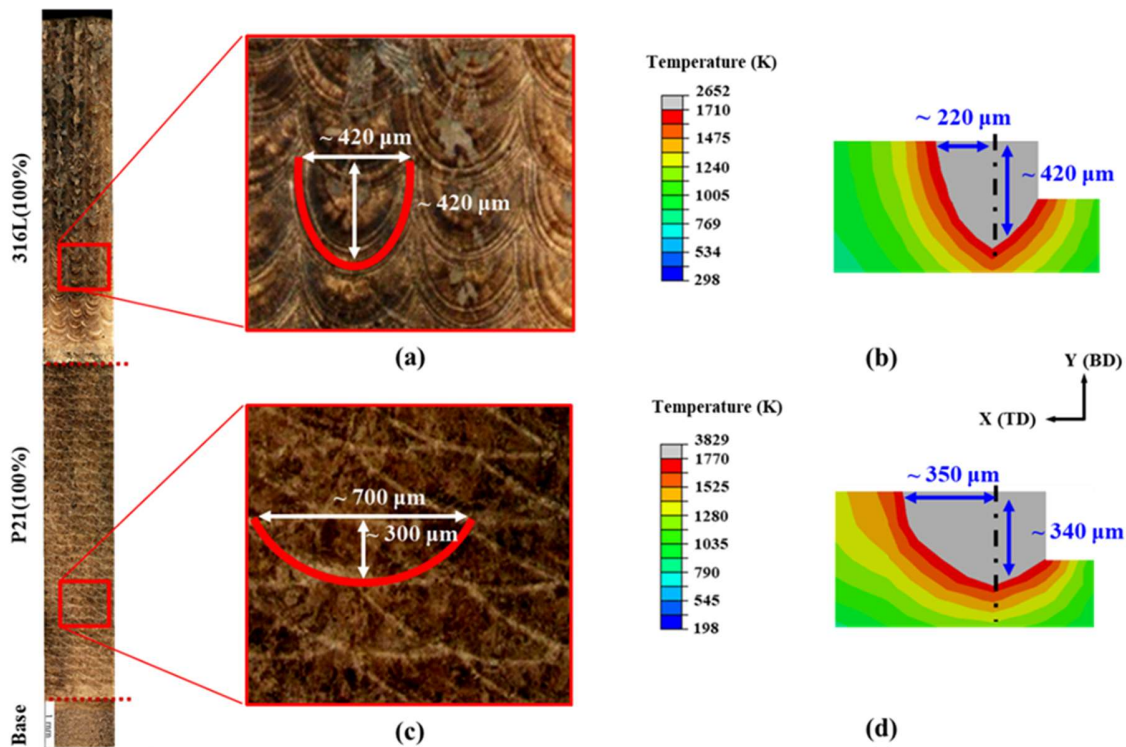


Fig. 4. 2 Melting pool sizes and morphologies of FGM structure by (a, c) macrostructure measurement and (b, d) simulation results for 316L and P21, respectively.

4.3. Inherent strains of each composition

The distributions of plastic strains for three compositions are shown in Fig. 4.3. The plastic strain of other compositions is not included because their distributions have similar trend compared with the distributions in Fig. 4.3. Firstly, the plastic strain distribution of single pass is generally constant in the middle region. It is confirmed that the length of deposition layer in meso-scale modeling is enough to make the thermal field and plastic strain reach the steady state. Secondly, in longitudinal direction (LD), the steady-state plastic strains of different passes are almost similar in each composition. In contrast, the distributions of different layers in transverse direction (TD) or building direction (BD) have a relatively large discrepancy, especially the plastic strains of pass 1 and 2 (bottom layer). The possible reason is that flat substrate provides a strong mechanical constraint to the bottom of the small printed part in TD and BD, instead the position of the melting area is always changed along the LD during the DED process. Furthermore, there is no pre-heating for the substrate which brings larger temperature gradient to the deposition of bottom layer. Compared to the bottom layer, the middle and top layers were built based on the bottom layer, which experience relatively weak constraint and small temperature gradient. Finally, the distributions of each composition also exist some difference. The plastic strains in TD or BD of P21 are similar for the middle and top layers. However, in 316L the relative values of different layers show a linear change with the increase of deposition layers, which seems to be the effect of layer-by-layer feature in AM process. According to the cross-sectional macrostructure of composition as mentioned before, the depth of melt pool of 316L is over 400 μm and the depth of P21 is only around 300 μm . It means the layer can be only slightly re-melted during the deposition

of subsequent layers in P21. While the layer could be mostly re-melted when the next layer is deposited for 316L.

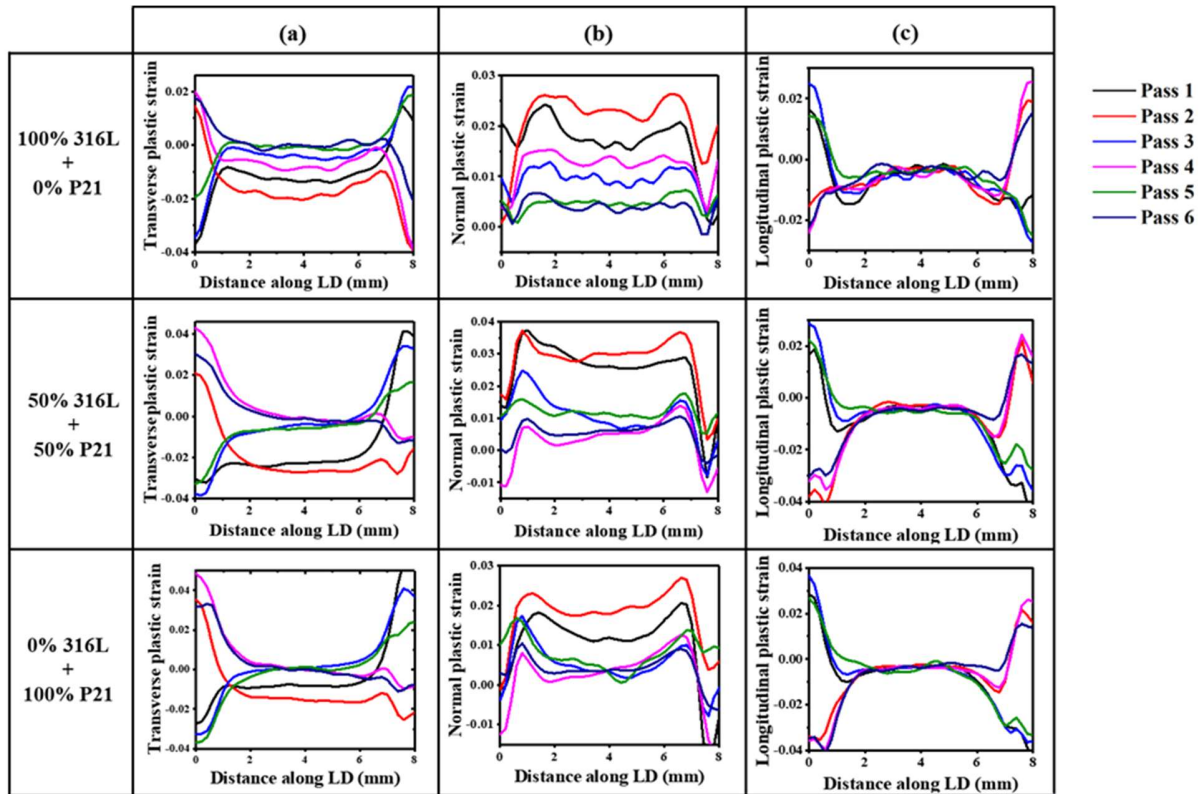


Fig. 4. 3 The plastic strain distributions in (a) TD, (b) BD and (c) LD along different passes of three compositions

For defining the inherent strains, the mean values were computed among the steady-state plastic strains of the middle layer and top layer. The values of plastic strain in the bottom layer were not included due to the large discrepancy in transverse and normal plastic strains. In other words, only the core area of the deposited part was considered to be utilized for extracting the inherent strains. The average inherent strains of each composition were depicted in the Fig. 4.4. There is a gradual increase in the magnitude of inherent strains with the adding of austenitic composition in general. It is reasonable because most of material properties also show the gradual

variation. Interestingly, a little decrease was found in the 50% 316L composition. The unique material properties as mentioned above and related process parameters can be responsible for this result.

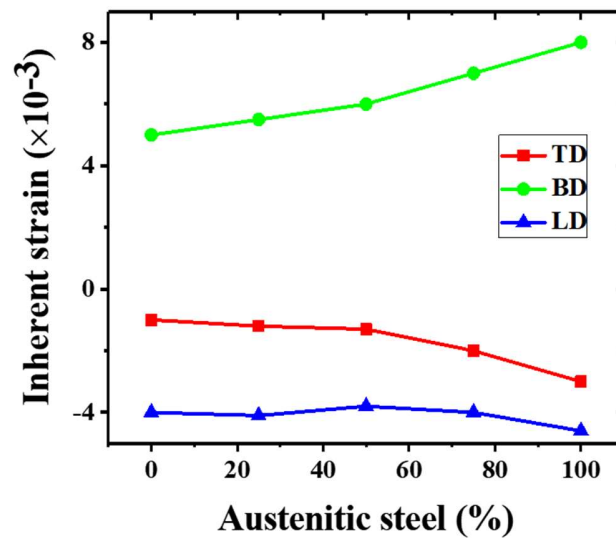


Fig. 4. 4 The inherent strains of each composition along the TD, BD and LD

4.4. Lumping layer method in case I

The two-dimensional maps of longitudinal residual stress obtained by different lumping layer strategies were compared with the results measured by contour method in Fig. 4.5. In the 1N strategy, the sharp transition in residual stress is easily observed around the interfaces of 316L and P21. And with the increase of numerical layer thickness, the high compressive residual stress around the interface continue to reduce. It seems that the large NLT for each composition can make the residual stress around the interface be over-estimated. For individual composition, the effect of layer-by-layer feature on residual stress can be well considered with small NLT. However, the compression in the middle part of the P21 composition shown in the results of contour method

was not captured by 3N and 6N accurately. It is regarded as the problem of coarse mesh in small NLT. The same mesh element size was applied to the model of 1N, 2N, 3N and 6N strategies. There are three mesh elements along thickness for each numerical layer in 2N and only single mesh element for each numerical layer in 6N. Thus, the mesh elements along the thickness were increased to 3 in the 3N3E and 6N3E strategies. As shown in the Fig. 4.5, the 3N3E and 6N3E have a better match with experimental result. Considering the computational cost, the residual stress in three normal directions along the center line depicted in Fig. 4.5 were extracted from the model with 3N3E strategy and compared with the results obtained by neutron diffraction for further investigation.

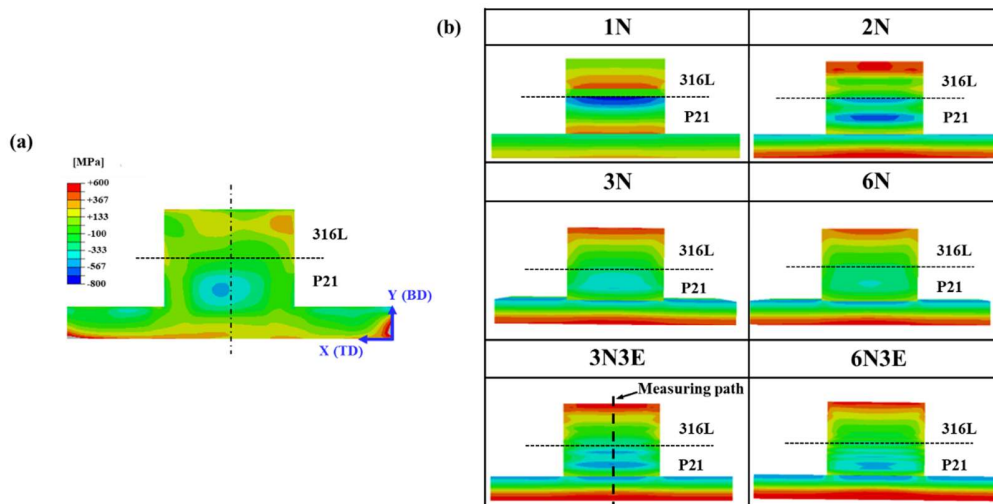


Fig. 4. 5 (a) Two-dimensional mapping of the residual stress distributions in LD obtained by contour method, and (b) predicted cross-sectional residual stress distribution in the FGM for case I by different layer lumping strategies.

As depicted in Fig. 4.6, the simulation results obtained by 3N3E show a good agreement with the neutron diffraction results. The stress profiles along LD shows “C” shape from the tensile stress about 300 MPa to the compressive stress up to the -470 MPa at the middle of the P21 part and then

returns to tension stress at the substrate. The stress profiles of TD also have the similar shape with smaller magnitude compared to the that of LD. In addition, the experimental residual stress along BD shows a little tensile stress near the top and bottom of the modeling. It may be mainly contributed to the thermal excursion and accumulation along BD during DED process or volume expansion caused by the martensite transformation in P21. The comparisons in Fig. 4.6 prove that 3N3E can well reproduce the experimental residual stress distribution in the case I, which were also applied to other three cases.

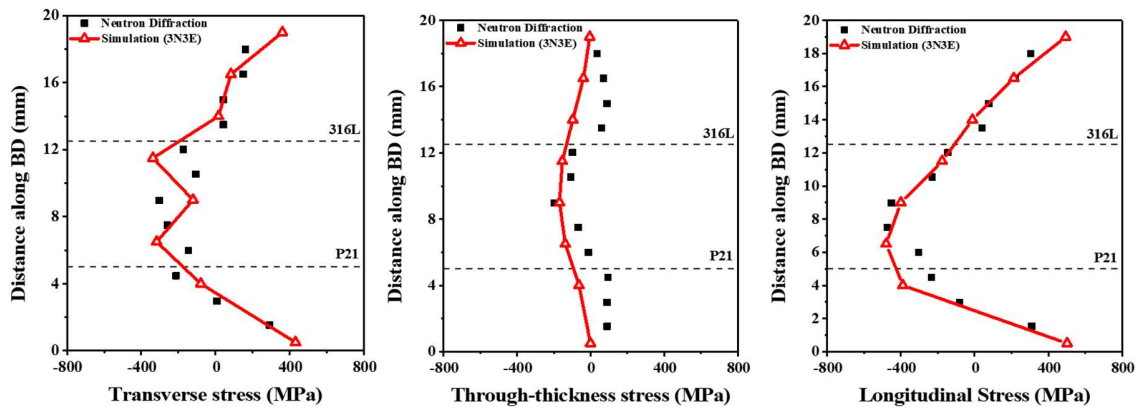


Fig. 4. 6 Residual stress distributions of the FGM for case I along the TD, BD and LD obtained from the measuring path as indicated in Fig. 9.

4.5. Residual stress and thermal distortion

Fig. 4.7 shows the predicted residual stress distribution by multiscale modeling, together with the experimental results obtained by the neutron diffraction, contour method and deep hole drilling. In case I, the overall trends are confirmed to be similar between the simulation and experiments. After adding the 50% 316L composition layer as intermediate layer in case II, the stress profiles significantly fluctuate with a sine-wave-like distribution through the thickness of the specimen.

The stress profile obtained by simulation has the similar shape with a little mismatch in P21 composition layer which shows the tensile stress. This is due to the consideration of a stress balancing mechanism of stress redistribution, in addition to the influence of volume expansion caused by the phase transformation. In the case III, although the range of stress has a little decrease in the simulation, the fluctuation also occurs at the 50% 316L composition layer. For the case IV was fabricated by the orthogonal scanning strategies, the transverse and longitudinal inherent strains could be regarded as the same value and the average of inherent strains along these two directions were mapped to the case IV. The stress profile is still similar with the case II and case III but indicates a smaller magnitude of the range of residual stress. There is a doubt that some certain composition is responsible for the fluctuation of the residual stress such as the 50% 316L composition. It was found that has the smallest magnitude among five calculated compositions. Therefore, a structure with new gradient path without 50% 316L composition was designed to perform the residual stress simulation to validate. As depicted in the Fig. 4.8(a), only 25% and 75% 316L composition layer was added between the P21 and 316L layer. These inherent strains of compositions were already verified by the experiments. In Fig. 4.8(b), compared with the residual stress of case III, the distribution of new gradient path was returned to the “C” shape and the fluctuation disappeared as expected. It reveals one advantage of the multiscale modeling on FGM is the effect of each composition on residual stress can be better investigated and it is meaningful in the design of the gradient path to reduce the residual stress.

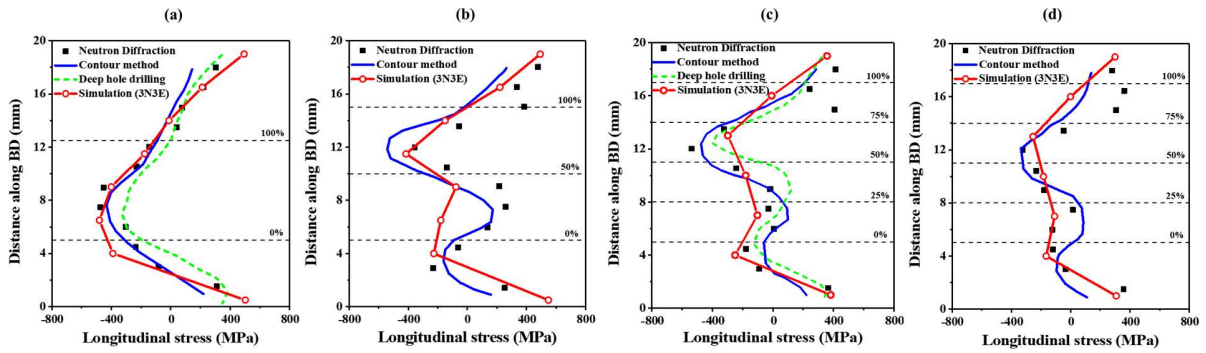


Fig. 4. 7 Through-thickness distributions of longitudinal stress obtained by neutron diffraction, contour method, deep hole drilling and multiscale simulation: (a) case I, (b) case II, (c) case III, and (d) case IV.

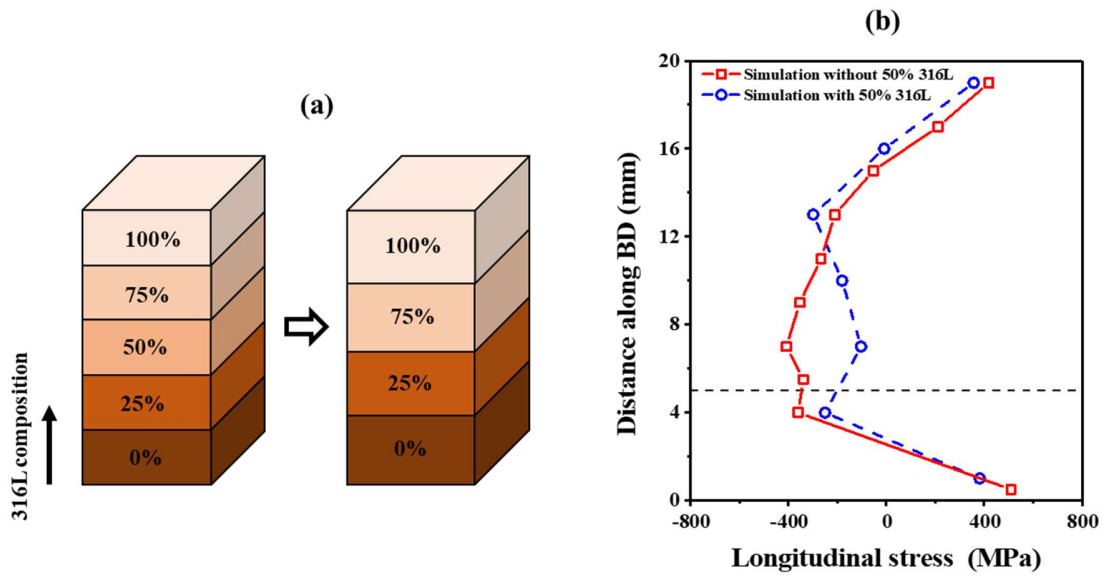


Fig. 4. 8 (a) Schematic of the new gradient path without the 50% 316L composition, and (b) Longitudinal residual stress distributions of two gradient paths (with and without 50% 316L composition)

The predictions of distortion for four cases are summarized in Fig. 4.9. The measuring path of distortion in simulation is shown in Fig. 4.9(a). The comparison between the experiment measurement and simulation are presented in Fig. 4.9(b-e). The thermal shrinkage of the center area makes the two sides be shrinking. The overall distortion shows good agreement between the experiment and simulation and maximum distortion is well captured. With the increase of the composition and orthogonal scanning strategy, the maximum value of distortion was reduced. Nevertheless, there is a little discrepancy in the middle area. It is considered that in the real fabrication process, the specimens were fabricated based on the substrate directly without any constraint. In simulation, however, the boundary conditions were applied to avoid the stiffness matrix singularity. It may lead to the difference of the inherent strains calculated in meso-scale model and affect the evolution of residual stress in macro-scale model.

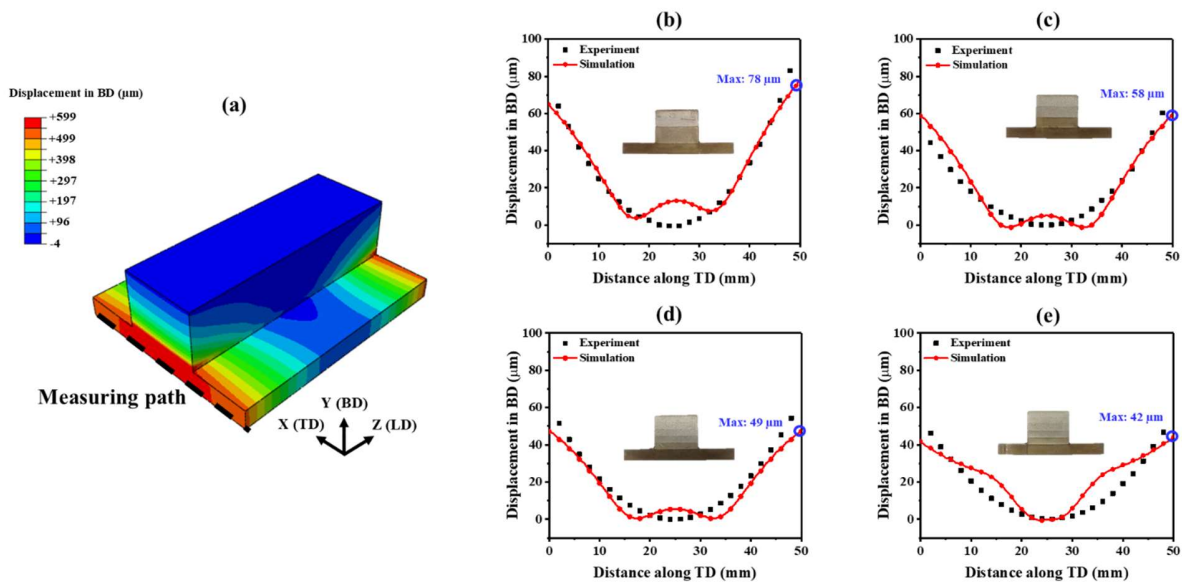


Fig. 4. 9 (a) Distortion field of case I and distortion profiles: (b) case I, (c) case II, (d) case III and (e) case IV.

As for the efficiency of the proposed model, the computation time of coupled thermo-mechanical analysis on the 3-layer model to determine the inherent strains and mapping inherent strains to the four cases for obtaining the residual stress distribution are plotted in Fig. 4.10. It took around 9h to perform the thermo-mechanical analysis on a 3-layer model with 12 passes. The four cases of specimens prepared in this research are 60-layer models, which can spend expensive computational cost to conduct such simulation directly. In contrast, after we defining the inherent strains of each composition, mapping to the different macro-scale structure have a significant reduction at computational time. Furthermore, with the addition of composition layer, the computational time experienced a large rise compared to case I due to the increase of activation steps and mesh numbers.

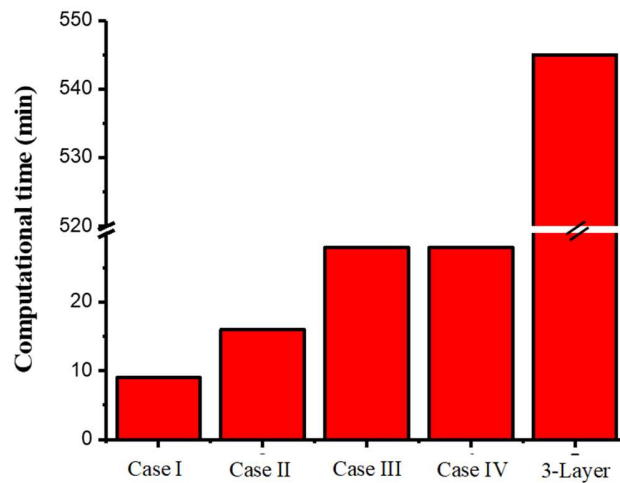


Fig. 4. 10 The computational time of the coupled thermo-mechanical analysis on the 3-layer meso-scale model and mapping inherent strains to different case

CHAPTER 5

CONCLUSIONS

The present study developed a multiscale modeling based on inherent strain method to predict the residual stress distribution in the functionally graded materials (FGMs) with different gradient path and scanning strategy. In thermo-mechanical analysis of meso-scale model, the inherent strains were extracted in the core area of the deposition. In addition, material properties of each composition were defined by thermodynamic calculations. By mapping inherent strains of different composition to the macro-scale model, the residual stress distributions in the FGMs were obtained by lumping layer methods accurately and efficiently. The little NLT for each composition can enlarge the interaction between the different composition.

With the different gradient path between the 316L and P21, the thermal distortions have been proved to reduce by adding the variety of compositions. However, the residual stress always shows a fluctuation around the intermediate layer which is not observed in the dissimilar structure (case I). The 50% 316L composition is considered to be responsible for the unexpected fluctuation due to its inherent strains has the smallest magnitude among the gradient path. A new gradient path without this composition were designed to prove it.

1. With the composition changes from the austenitic to ferritic steel, most of temperature-dependent material properties show a linear change. But for yield stress, the intermediate parts showed the high value (970 MPa) closed to P21 (MPa), rather than a median value between the values for the 316L and P21 layers.

2. Cross-sectional macrostructure of each composition were obtained to calibrate the thermal model. The melt pool in 316L part is comparatively short in width and deep in depth compared with P21 part.

3. The residual stress distribution obtained by 1P3L lumping layer strategies shows a good agreement with experimental results. The “C” shape stress profile in case I and sine-wave-like distribution in other cases were well captured.

4. In predicting the thermal distortion, the multiscale modeling also has a good accuracy. And with the increase of the composition parts, the maximum value of distortion reduces from 78 μm to 42 μm .

The proposed model can offer a particular view for studying about the residual stress, the FGM structure cannot be simply considered to minimize the residual stress distribution compared to dissimilar structure. The unexpected fluctuation may be caused by some unique compositions. For the mechanical properties of the same composition can be affected by various process parameters in AM.

REFERENCES

- [1] B. Kieback, A. Neubrand, H. Riedel, Processing techniques for functionally graded materials, *Materials Science and Engineering: A*. 362 (2003) 81–106. [https://doi.org/10.1016/S0921-5093\(03\)00578-1](https://doi.org/10.1016/S0921-5093(03)00578-1).
- [2] R.M. Mahamood, E.T. Akinlabi, *Functionally Graded Materials*, Springer International Publishing, Cham, 2017. <https://doi.org/10.1007/978-3-319-53756-6>.
- [3] J.F. Groves, H.N.G. Wadley, Functionally graded materials synthesis via low vacuum directed vapor deposition, *Composites Part B: Engineering*. 28 (1997) 57–69. [https://doi.org/10.1016/S1359-8368\(96\)00023-6](https://doi.org/10.1016/S1359-8368(96)00023-6).
- [4] C. Chenglin, Z. Jingchuan, Y. Zhongda, W. Shidong, Hydroxyapatite–Ti functionally graded biomaterial fabricated by powder metallurgy, *Materials Science and Engineering: A*. 271 (1999) 95–100. [https://doi.org/10.1016/S0921-5093\(99\)00152-5](https://doi.org/10.1016/S0921-5093(99)00152-5).
- [5] Z. Qiao, J. Räthel, L.M. Berger, M. Herrmann, Investigation of binderless WC–TiC–Cr₃C₂ hard materials prepared by spark plasma sintering (SPS), *International Journal of Refractory Metals and Hard Materials*. 38 (2013) 7–14. <https://doi.org/10.1016/J.IJRMHM.2012.12.002>.
- [6] T.P.D. Rajan, R.M. Pillai, B.C. Pai, Characterization of centrifugal cast functionally graded aluminum-silicon carbide metal matrix composites, *Materials Characterization*. 61 (2010) 923–928. <https://doi.org/10.1016/J.MATCHAR.2010.06.002>.
- [7] C. Zhang, F. Chen, Z. Huang, M. Jia, G. Chen, Y. Ye, Y. Lin, W. Liu, B. Chen, Q. Shen, L. Zhang, E.J. Lavernia, Additive manufacturing of functionally graded materials: A review,

Materials Science and Engineering: A. 764 (2019) 138209.

<https://doi.org/10.1016/J.MSEA.2019.138209>.

- [8] L. Yan, Y. Chen, F. Liou, Additive manufacturing of functionally graded metallic materials using laser metal deposition, *Additive Manufacturing*. 31 (2020) 100901.
<https://doi.org/10.1016/J.ADDMA.2019.100901>.
- [9] G.H. Loh, E. Pei, D. Harrison, M.D. Monzón, An overview of functionally graded additive manufacturing, *Additive Manufacturing*. 23 (2018) 34–44.
<https://doi.org/10.1016/J.ADDMA.2018.06.023>.
- [10] L.D. Bobbio, R.A. Otis, J.P. Borgonia, R.P. Dillon, A.A. Shapiro, Z.K. Liu, A.M. Beese, Additive manufacturing of a functionally graded material from Ti-6Al-4V to Invar: Experimental characterization and thermodynamic calculations, *Acta Materialia*. 127 (2017) 133–142.
<https://doi.org/10.1016/J.ACTAMAT.2016.12.070>.
- [11] B.E. Carroll, R.A. Otis, J.P. Borgonia, J.O. Suh, R.P. Dillon, A.A. Shapiro, D.C. Hofmann, Z.K. Liu, A.M. Beese, Functionally graded material of 304L stainless steel and Inconel 625 fabricated by directed energy deposition: Characterization and thermodynamic modeling, *Acta Materialia*. 108 (2016) 46–54. <https://doi.org/10.1016/J.ACTAMAT.2016.02.019>.
- [12] A. Ben-Artzy, A. Reichardt, J.P. Borgonia, R.P. Dillon, B. McEnerney, A.A. Shapiro, P. Hosemann, Compositionally graded SS316 to C300 Maraging steel using additive manufacturing, *Materials & Design*. 201 (2021) 109500.
<https://doi.org/10.1016/J.MATDES.2021.109500>.

- [13] J.L. Bartlett, X. Li, An overview of residual stresses in metal powder bed fusion, *Additive Manufacturing*. 27 (2019) 131–149. <https://doi.org/10.1016/J.ADDMA.2019.02.020>.
- [14] K. An, L. Yuan, L. Dial, I. Spinelli, A.D. Stoica, Y. Gao, Neutron residual stress measurement and numerical modeling in a curved thin-walled structure by laser powder bed fusion additive manufacturing, *Materials & Design*. 135 (2017) 122–132. <https://doi.org/10.1016/J.MATDES.2017.09.018>.
- [15] Z. Wang, A.D. Stoica, D. Ma, A.M. Beese, Stress relaxation in a nickel-base superalloy at elevated temperatures with in situ neutron diffraction characterization: Application to additive manufacturing, *Materials Science and Engineering: A*. 714 (2018) 75–83. <https://doi.org/10.1016/J.MSEA.2017.12.058>.
- [16] Z. Wang, E. Denlinger, P. Michaleris, A.D. Stoica, D. Ma, A.M. Beese, Residual stress mapping in Inconel 625 fabricated through additive manufacturing: Method for neutron diffraction measurements to validate thermomechanical model predictions, *Materials & Design*. 113 (2017) 169–177. <https://doi.org/10.1016/J.MATDES.2016.10.003>.
- [17] T. Simson, A. Emmel, A. Dwars, J. Böhm, Residual stress measurements on AISI 316L samples manufactured by selective laser melting, *Additive Manufacturing*. 17 (2017) 183–189. <https://doi.org/10.1016/J.ADDMA.2017.07.007>.
- [18] B. Vrancken, V. Cain, R. Knutsen, J. van Humbeeck, Residual stress via the contour method in compact tension specimens produced via selective laser melting, *Scripta Materialia*. 87 (2014) 29–32. <https://doi.org/10.1016/J.SCRIPTAMAT.2014.05.016>.

- [19] E.R. Denlinger, J.C. Heigel, P. Michaleris, T.A. Palmer, Effect of inter-layer dwell time on distortion and residual stress in additive manufacturing of titanium and nickel alloys, *Journal of Materials Processing Technology*. 215 (2015) 123–131.
<https://doi.org/10.1016/J.JMATPROTEC.2014.07.030>.
- [20] Y. Li, K. Zhou, P. Tan, S.B. Tor, C.K. Chua, K.F. Leong, Modeling temperature and residual stress fields in selective laser melting, *International Journal of Mechanical Sciences*. 136 (2018) 24–35. <https://doi.org/10.1016/J.IJMECSCI.2017.12.001>.
- [21] Z. Luo, Y. Zhao, A survey of finite element analysis of temperature and thermal stress fields in powder bed fusion Additive Manufacturing, *Additive Manufacturing*. 21 (2018) 318–332.
<https://doi.org/10.1016/J.ADDMA.2018.03.022>.
- [22] H. Huang, N. Ma, J. Chen, Z. Feng, H. Murakawa, Toward large-scale simulation of residual stress and distortion in wire and arc additive manufacturing, *Additive Manufacturing*. 34 (2020) 101248. <https://doi.org/10.1016/J.ADDMA.2020.101248>.
- [23] Y. Cao, X. Lin, N. Kang, L. Ma, L. Wei, M. Zheng, J. Yu, D. Peng, W. Huang, A novel high-efficient finite element analysis method of powder bed fusion additive manufacturing, *Additive Manufacturing*. 46 (2021) 102187. <https://doi.org/10.1016/J.ADDMA.2021.102187>.
- [24] J. Irwin, P. Michaleris, A Line Heat Input Model for Additive Manufacturing, *Journal of Manufacturing Science and Engineering*. 138 (2016). <https://doi.org/10.1115/1.4033662>.
- [25] M. Chiumenti, E. Neiva, E. Salsi, M. Cervera, S. Badia, J. Moya, Z. Chen, C. Lee, C. Davies, Numerical modelling and experimental validation in Selective Laser Melting, *Additive Manufacturing*. 18 (2017) 171–185. <https://doi.org/10.1016/J.ADDMA.2017.09.002>.

- [26] Y. Ueda, K. Fukuda, K. Nakacho, S. Endo, A New Measuring Method of Residual Stresses with the Aid of Finite Element Method and Reliability of Estimated Values, *Journal of the Society of Naval Architects of Japan*. 1975 (1975) 499–507.
https://doi.org/10.2534/jjasnaoe1968.1975.138_499.
- [27] M.R. Hill, D. v Nelson, THE INHERENT STRAIN METHOD FOR RESIDUAL STRESS DETERMINATION AND ITS APPLICATION TO A LONG WELDED JOINT, n.d.
- [28] M. Bugatti, Q. Semeraro, Limitations of the inherent strain method in simulating powder bed fusion processes, *Additive Manufacturing*. 23 (2018) 329–346.
<https://doi.org/10.1016/J.ADDMA.2018.05.041>.
- [29] X. Liang, L. Cheng, Q. Chen, Q. Yang, A.C. To, A modified method for estimating inherent strains from detailed process simulation for fast residual distortion prediction of single-walled structures fabricated by directed energy deposition, *Additive Manufacturing*. 23 (2018) 471–486.
<https://doi.org/10.1016/J.ADDMA.2018.08.029>.
- [30] Q. Chen, X. Liang, D. Hayduke, J. Liu, L. Cheng, J. Oskin, R. Whitmore, A.C. To, An inherent strain based multiscale modeling framework for simulating part-scale residual deformation for direct metal laser sintering, *Additive Manufacturing*. 28 (2019) 406–418.
<https://doi.org/10.1016/J.ADDMA.2019.05.021>.
- [31] X. Liang, W. Dong, Q. Chen, A.C. To, On incorporating scanning strategy effects into the modified inherent strain modeling framework for laser powder bed fusion, *Additive Manufacturing*. 37 (2021) 101648. <https://doi.org/10.1016/J.ADDMA.2020.101648>.

- [32] X. Liang, D. Hayduke, A.C. To, An enhanced layer lumping method for accelerating simulation of metal components produced by laser powder bed fusion, *Additive Manufacturing*. 39 (2021) 101881. <https://doi.org/10.1016/J.ADDMA.2021.101881>.
- [33] X. Liang, W. Dong, S. Hinnebusch, Q. Chen, H.T. Tran, J. Lemon, L. Cheng, Z. Zhou, D. Hayduke, A.C. To, Inherent strain homogenization for fast residual deformation simulation of thin-walled lattice support structures built by laser powder bed fusion additive manufacturing, *Additive Manufacturing*. 32 (2020) 101091. <https://doi.org/10.1016/J.ADDMA.2020.101091>.
- [34] I. Setien, M. Chiumenti, S. van der Veen, M. San Sebastian, F. Garcíandía, A. Echeverría, Empirical methodology to determine inherent strains in additive manufacturing, *Computers & Mathematics with Applications*. 78 (2019) 2282–2295. <https://doi.org/10.1016/J.CAMWA.2018.05.015>.
- [35] Y. Wang, Q. Li, L. Qian, Y. Yang, A modified inherent strain model with consideration of the variance of mechanical properties in metal additive manufacturing, *Journal of Manufacturing Processes*. 72 (2021) 115–125. <https://doi.org/10.1016/J.JMAPRO.2021.09.059>.
- [36] T. Mukherjee, J.S. Zuback, W. Zhang, T. DebRoy, Residual stresses and distortion in additively manufactured compositionally graded and dissimilar joints, *Computational Materials Science*. 143 (2018) 325–337. <https://doi.org/10.1016/J.COMMATSCI.2017.11.026>.
- [37] L. Li, X. Zhang, W. Cui, F. Liou, W. Deng, W. Li, Temperature and residual stress distribution of FGM parts by DED process: modeling and experimental validation, *The International Journal of Advanced Manufacturing Technology*. 109 (2020) 451–462. <https://doi.org/10.1007/s00170-020-05673-4>.

- [38] X. Zhang, L. Li, T. Pan, Y. Chen, Y. Zhang, W. Li, F. Liou, Additive manufacturing of copper-tool steel dissimilar joining: Experimental characterization and thermal modeling, *Materials Characterization*. 170 (2020) 110692. <https://doi.org/10.1016/J.MATCHAR.2020.110692>.
- [39] D.K. Kim, W. Woo, E.Y. Kim, S.H. Choi, Microstructure and mechanical characteristics of multi-layered materials composed of 316L stainless steel and ferritic steel produced by direct energy deposition, *Journal of Alloys and Compounds*. 774 (2019) 896–907. <https://doi.org/10.1016/J.JALLCOM.2018.09.390>.
- [40] W. Woo, D.K. Kim, E.J. Kingston, V. Luzin, F. Salvemini, M.R. Hill, Effect of interlayers and scanning strategies on through-thickness residual stress distributions in additive manufactured ferritic-austenitic steel structure, *Materials Science and Engineering: A*. 744 (2019) 618–629. <https://doi.org/10.1016/J.MSEA.2018.12.078>.
- [41] N. Saunders, U.K.Z. Guo, X. Li, A.P. Miodownik, J.-Ph. Schillé, Using JMatPro to model materials properties and behavior, *JOM*. 55 (2003) 60–65. <https://doi.org/10.1007/s11837-003-0013-2>.
- [42] Z. Fan, P. Tsakirooulos, A.P. Miodownik, A generalized law of mixtures, *Journal of Materials Science*. 29 (1994) 141–150. <https://doi.org/10.1007/BF00356585>.
- [43] J. Goldak, A. Chakravarti, M. Bibby, A new finite element model for welding heat sources, *Metallurgical Transactions B*. 15 (1984) 299–305. <https://doi.org/10.1007/BF02667333>.